

Magneto-electric Tuning of Pinning-Type Permanent Magnets through Atomic-Scale Engineering of Grain Boundaries

Xinglong Ye^{1*}, Fengkai Yan²◆, Lukas Schaefer³, Di Wang^{1,4}, Holger Geßwein⁵, Wu Wang^{1,†},
Mohammed Reda Chellali¹, Leigh T. Stephenson², Konstantin Skokov³, Oliver Gutfleisch³, Dierk Raabe²,
Horst Hahn¹, Baptiste Gault^{2,6*}, Robert Kruk¹

¹ Institute of Nanotechnology, Karlsruhe Institute of Technology (KIT), Eggenstein-Leopoldshafen, Germany

² Department of Microstructure Physics and Alloy Design, Max-Planck-Institut für Eisenforschung GmbH (MPIE), Düsseldorf, Germany.

³ Department of Material Science, Technical University Darmstadt, Darmstadt, Germany

⁴ Karlsruhe Nano Micro Facility, Karlsruhe Institute of Technology (KIT), Karlsruhe, Germany

⁵ Institute for Applied Materials, Karlsruhe Institute of Technology, Eggenstein-Leopoldshafen, Germany.

⁶ Department of Materials, Imperial College London, London, UK

Corresponding authors. Email: xing-long.ye@kit.edu; b.gault@mpie.de

◆ now at Institute of Metal Research, Chinese Academy of Science, Shenyang, China

† now at Department of Physics, Southern University of Science and Technology, Shenzhen, China.

Abstract

Pinning-type magnets maintaining high coercivity, i.e. the ability to sustain magnetization, at high temperature are at the core of thriving clean-energy technologies. Among these, $\text{Sm}_2\text{Co}_{17}$ -based magnets are excellent candidates owing to their high-temperature stability. However, despite decades of efforts to optimize the intragranular microstructure, the coercivity currently only reaches 20~30% of the theoretical limits. Here, the roles of the grain-interior nanostructure and the grain boundaries in controlling coercivity are disentangled by an emerging magneto-electric approach. Through hydrogen charging/discharging by applying voltages of only ~ 1 V, the coercivity is reversibly tuned by an unprecedented value of ~ 1.3 T. In situ magneto-structural measurements and atomic-scale tracking of hydrogen atoms reveal that the segregation of hydrogen atoms at the grain boundaries, rather than the change of the crystal structure, dominates the reversible and substantial change of coercivity. Hydrogen lowers the local magnetocrystalline anisotropy and facilitates the magnetization reversal starting from the grain boundaries. Our study reveals the previously neglected critical role of grain boundaries in the conventional magnetisation-switching paradigm, suggesting a critical reconsideration of strategies to overcome the coercivity limits in permanent magnets, via for instance atomic-scale grain boundary engineering.

Consequently present work . (200 words)

Key words: Magneto-electric, Permanent magnets, Hydrogen, Grain boundary

Introduction

Permanent magnets with the ability to maintain their magnetization, i.e. a property referred to as coercivity, at high temperatures are crucial for the flourishing clean energy technologies such as electric vehicles and wind powers^{1,2}. In this regard, the pinning-type magnets, in which the coercivity arises from the pinning of magnetic domain walls at nano-precipitates within the grain,⁶⁻⁸ are most promising. As an example, the Sm₂Co₁₇-based magnet is the only candidate for use in electric motors working above 300 °C owing to its excellent temperature stability. Its coercivity is usually believed to be controlled exclusively by domain-wall pinning because of the nano-scale cellular microstructure within the grain⁹⁻¹³, while the initial demagnetization at grain boundaries is considered irrelevant. However, despite intensive efforts to optimize its intra-granular microstructure, the coercivity currently only reaches 20-30% of the theoretical anisotropy field.^{1,14,15} Hence, it inevitably opens the question about the possible influence of grain boundaries during the magnetization reversal of the material.

The role of grain boundaries in pinning-type magnets may be understood if they can be modified separately from the grain interior, in conjunction with measuring the associated coercivity change. Traditional processing approaches, such as heat treatments¹³, plastic deformation¹⁶ and alloying^{9,17}, can dramatically change the coercivity. However, these approaches often induce irreversible modification (or destruction) of the microstructure both in grain boundaries and grain interior, obscuring the assessment of their respective impact on coercivity. Consequently, decoupling the separate roles of the grain boundary and the grain interior in magnetization reversal becomes technically challenging.

It has recently been demonstrated that the magneto-electric approach can reversibly modify the magnetic properties of materials with external voltages without changing the microstructure^{8,19}. For instance, voltage-driven proton pumping and the voltage-controlled hydrogen insertion/extraction can substantially tune the coercivity of ferromagnetic metals.^{20,21} Owing to different affinities of hydrogen atoms to the microstructural defects, hydrogen atoms are expected to diffuse first along the grain boundaries, and, then into the grain interior.^{22,23} This sequential diffusion, if controlled, offers an opportunity to decouple the roles of the grain boundary and the grain interior, if the associated coercivity change is monitored at each step. Here, by employing electrochemically-controlled hydrogen charging/discharging, we tuned the coercivity of the Sm₂Co₁₇-based hard magnet by ~1.3 T, the largest values ever achieved by magneto-electric approaches. The combined in situ magneto-structural measurements and atomic-scale mapping of hydrogen distribution²⁴ reveal that hydrogen atoms strongly segregate at grain boundaries, which weakens the local magnetic anisotropy and accounts for the predominant change of coercivity. Our study opens a way to achieve giant magnetoelectric effects by atomic-scale engineering of grain boundaries, and unveils the critical role of grain boundaries in limiting pinning-type magnet's performance pointing the way forward for future optimisation strategies.

Results

Magneto-optical observation of magnetization reversal

We used commercial Sm₂Co₁₇-based permanent magnets with compositions of Sm(Co_{0.766}

$\text{Fe}_{0.116}\text{Cu}_{0.088}\text{Zr}_{0.029}\text{Co}_{7.35}$ (hereafter referred to as $\text{SmCo}_{7.35}$ sample) (**Table S1**). The hysteresis loop shows a coercivity of ~ 2.8 T (**Fig. 1A**). By magneto-optical Kerr effect (MOKE) microscopy, we observed its magnetization reversal process under demagnetization fields. Prior to MOKE imaging, the sample was fully magnetized at -6.8 T (**Fig. 1B**), and the domain structure imaged with the c-axis in the viewing plane.

At a demagnetization field of 1.5 T, the sample retained its fully-magnetized state (**Fig. 1C**). When the field increased to 2 T, the reversed domains started to appear at grain boundaries (**Fig. 1D**), and at 2.2 T expanded into the interior of the grains (**Fig. 1E**). With further increasing field, the magnetic domains moved massively into the grain (**Fig. 1F**). At 3.0 T, only a few residual domains were un-reversed (**Fig. 1G**). These observations demonstrate the initial nucleation of magnetic domains at grain boundaries before their growth into the grain interior.

Reversible modification of coercivity by non-destructive hydrogen charging/discharging

We employed an electrochemical three-electrode cell to charge/discharge the $\text{SmCo}_{7.35}$ sample with hydrogen atoms (**Fig. S1**). In this setup, the as-prepared electrode with the $\text{SmCo}_{7.35}$ particles was the working electrode and 1 M KOH aqueous solution the electrolyte (**Fig. S2**). During hydrogen charging, the electrochemical reduction of water molecules on the metal surface provides the hydrogen ad-atoms that subsequently diffuse into the material. Conversely, during the discharging, the hydrogen atoms on the surface (H_{ads}) were oxidized and removed, resulting in hydrogen desorption. Based on the measured cyclic voltammogram (**Fig. S3**), we used the voltages steps of -1.2 V and -0.4 V to charge and discharge the sample, respectively.

We explored the response of the coercivity of the as-prepared $\text{SmCo}_{7.35}$ sample to hydrogen charging/discharging by *in situ* superconducting quantum interference device (SQUID). The coercivity of the as-prepared sample was ~ 2.3 T (**Fig. 2A**), slightly lower than that of the bulk-form pristine sample (~ 2.8 T) (**Fig. 1A**). After charging at -1.2 V for one hour, the coercivity drastically decreased to ~ 1.0 T. We monitored the recovery of the coercivity during the discharging process by continuously recording the hysteresis loops. The coercivity increased monotonically with the discharging time (**Fig. 2A**), and regained most of its initial value in the early stage of the discharging process, reaching ~ 1.9 T within 10 hours (**inset in Fig. 2A**). After a prolonged time of discharging (~ 60 hours), the coercivity fully recovered.

In parallel, we studied the dynamics of the hydrogen charging/discharging process by observing the evolution of crystal structure with *in situ* X-ray diffraction (XRD) in transmission mode (**Fig. 2B**). Upon hydrogen-charging, all diffraction peaks were shifted to lower angles, and after one hour, the positions of the diffraction peaks stayed unchanged, indicating the complete charging of the whole sample. In the discharging process, two stages were discerned. First, strikingly, only a negligible shift of the peaks was observed over the first 10 hours (**Fig. 2C**), indicating that the bulk material is still charged with hydrogen atoms. Second, only after about 80 hours of discharging the peaks recovered to their original positions. This observation is in strong contrast with the substantial change in coercivity over the corresponding period (**Inset in Fig. 2A**). It suggests that the predominant coercivity

change is not ascribed to the slow hydrogen desorption from the volume of the material. Since the predominant change of coercivity does not arise from the volumetric slow diffusion of hydrogen atoms, we expect a relatively fast response of magnetization reversal to hydrogen charging (**Fig. 2C**). We first magnetized the as-prepared sample with 6.8 T (point ① in the inset). Then, the magnetic field was reversed to -1.1 T (point ②), smaller than the coercivity of the pristine sample (~2.3 T) and therefore, the magnetization remained positive and nearly constant. Upon hydrogen charging by applying -1.2 V (point ③), the magnetization decreased immediately and abruptly, and flipped from positive to negative in ~10 minutes. The magnetization started to level off after ~4 hours. The immediate response of magnetization reversal to the voltage stimulus confirms the existence of relatively fast diffusion path of hydrogen atoms.

Atomic-scale tracking of hydrogen atoms within the hierarchical microstructure

We carried out multi-scale multi-microscopy mapping of the micro- and nano-structural features to rationalize the fast diffusion pathways of hydrogen atoms. Optical microscopy (**Fig. 3A, Fig. 1**) showed that the sample was polycrystalline with grains of ~26 μm separated by high-angle grain boundaries (HAGBs). The grains were further divided into sub-grains by low-angle grain boundaries (LAGBs) as shown by electron back-scattered imaging (**Fig. 3B**). Inside the grain transmission electron microscopy shows the typical cellular structure, composed of the matrix cell with sizes of ~40 nm, the cell boundary and the Zr-rich lamellae crossing the cellular structure (TEM, **Fig. 3C, S4**). After tilting the c-axis of the specimen out of the viewing plane, high-resolution TEM and the corresponding selected area electron diffraction (SAED) showed that the matrix phase is $\text{Sm}_2\text{Co}_{17}$ (rhombohedral $\text{Th}_2\text{Zn}_{17}$ type) and the cell boundary phase SmCo_5 (hexagonal CaCu_5 type) (**Fig. 3D**). This hierarchical micro- and nanostructure matches previous reports⁹⁻¹³.

We used atom probe tomography (APT) to locate hydrogen atoms and deuterium atoms within the hierarchical microstructure of the deuterium-charged samples. Isotopic marking by deuterium atoms (D) minimized the influence of residual hydrogen in the atom probe. We first analysed a specimen containing a HAGB (**Fig. S5, S6**). The element-specific atom maps in **Fig. 4A** reveal the Cu-rich cell boundaries, the matrix cells and the Zr-rich platelets, matching TEM results. Three-dimensional reconstruction shows that D mostly segregates in a 10–12 nm thick layer at HAGB, reaching a concentration of approx. 3.5 at% (**Fig. 4A**). A close face-on view (**Fig. 4B**) reveals that D segregates at the intersection of the cell boundaries with the HAGB. In the cells and cell boundaries, a very limited amount of D was detected within the structure close to the detection limit, with no noticeable partitioning difference between them (**Fig. S6**). In addition, deuterium atoms appear slightly depleted from the Zr-phase.

We then performed another analysis targeting LAGBs (**Fig. 4C, D, S7**). Again, deuterium appears depleted in the Z-phase, and no preferential segregation within cells and the cell boundaries (**Fig. S8**). Yet again, a strong segregation of deuterium at LAGB was observed. The corresponding top-view shows a series of linear features highlighted by a set of 0.35 at.% D iso-composition surfaces, which are likely the dislocations that constitute the LAGB²⁶. The D-concentration at these dislocations can

reach up to 0.4 at% D, and H up to 4–5 at%. Importantly, the cell edges are all connected to these dislocations and the cell structure stops abruptly at LAGB (**Fig. 4D**).

Discussion

The observation of hydrogen/deuterium segregation at GB regions (**Fig. 4**), coupled with *in situ* XRD, detecting no volumetric structural change (**Fig. 2B**), suggests that the substantial change of coercivity in the early stage of discharging process arises from the desorption of hydrogen atoms from GBs. The ability to modulate the coercivity by only charging/discharging GBs enables the fast control of coercivity, as verified by the immediate start of magnetization reversal upon hydrogen charging (**Fig. 2B**). The herein identified crucial role of grain boundary in controlling the coercivity explains why reducing the volume fraction of grain boundaries²⁷ or optimising the cellular structure near the grain boundary²⁸ can increase the coercivity of Sm₂Co₁₇-based magnets. Below we discuss how hydrogen segregation at GBs changes the coercivity, starting with the microstructural features near GBs.

Three microstructural features distinguish the GB region from the grain interior. First, compared with the continuous cellular structure in the grain interior (bottom part in **Fig. 4C**), the cell boundaries are broken and terminated near GBs (**Fig. 4A, C, D**). Second, the typical cell size and shape in the grain is approx. 40 nm and with a regular shape, but becomes larger and strongly elongated near GBs (**Fig. 4**). These results agree with recent TEM reports that the incomplete cellular structure near GBs extend towards the sub-micrometer scale^{29,30}. Third, the composition profiles (**Fig. S6, S8**) show that the SmCo₅ phase contains almost twice as much Cu near the grain boundary, i.e. 30 at.% compared with 15 at.% in the grain interior.

The observed different cellular structure and microchemistry near GBs significantly reduces the local nucleation field required for magnetization reversal. According to the micromagnetic theory, the critical nucleation field, H_n , can be described by¹⁴

$$H_n = \frac{1}{2M_s\Delta} (\gamma_{SmCo_5} - \gamma_{GB}) - DM_s \quad (1)$$

in which Δ is the width of the transition region where the domain-wall energy changes from γ_{GB} in the grain boundary to γ_{SmCo_5} in the cell boundary, and D is the demagnetizing factor. The SmCo₅ phase has much larger magnetocrystalline anisotropy than GBs, and determines the domain-wall energy difference, $(\gamma_{SmCo_5} - \gamma_{GB})$. Near GBs the Cu concentration in the SmCo₅ phase becomes twice that in the grain interior, which substantially reduces its magnetocrystalline anisotropy^{31,32} and thus the domain wall energy, γ_{SmCo_5} . In addition, the disrupted SmCo₅ phase allows the easy movement of domain walls through the matrix phase, triggering a macroscopic magnetization reversal. These account for the preferential nucleation of reversed domains near GBs (**Fig. 1**). Moreover, when the SmCo₅ phase was charged with hydrogen atoms, its magnetocrystalline anisotropy will decrease by ~40%²⁰. This further decreases the domain-wall energy of the SmCo₅ phase and the nucleation field. Besides, hydrogen segregation may enlarge the transition region (Δ) between GBs and the SmCo₅ phase with its continuous concentration change and reduce the nucleation field. Hence, hydrogen segregation acts here as a tool to further weaken the nucleation field of the GB region and amplify its

effect in initiating the magnetization reversal. Next, we consider the mechanism behind the propagation of the initially-nucleated magnetic domains near GBs into the grain interior.

In the grain interior, the continuous network of the SmCo_5 phase subdivides the individual grains of the $\text{Sm}_2\text{Co}_{17}$ matrix into a nanoscale cellular structure, rendering them into classical pinning-type magnets. However, the models to explain their magnetization reversal assume that grain boundaries should be non-ferromagnetic and one-to-two atomic layers thick to reduce the associated stray field negligibly^{14,33}. This is not the case in the current material because of the expanded region near GBs with the disintegrated cellular structure and different microchemistry. We can describe the demagnetization process of the whole grain triggered by the initial demagnetization near GB as follows. The local magnetic field is a superposition of the external field H_{ext} and the local demagnetization field, $N'M$, where N' is the local or effective demagnetization factor and M the net magnetization of the sample. The latter can be significantly inhomogeneous, and reach values much larger than the net demagnetization field³, $H_D = NM$, N being the demagnetization factor of the sample (3). As discussed earlier, the nucleation field of the GB region, $H_{c,GB}$, is much smaller than H_c of the grain interior, $H_{c,g}$. Under a small external field, we have $H_{c,g} > H_{c,GB} > H_{ext} + NM$. As the local magnetic field, $H_{ext} + NM$, approaches $H_{c,GB}$, the initial nucleation of magnetic domains occurs near GBs (**Fig. 1**), producing a local demagnetization field, $N'M_s$, where M_s is spontaneous magnetization of the main $\text{Sm}_2\text{Co}_{17}$ phase. Then, the adjacent inner layer with higher coercivity, $H_{c,g}$, is under the higher magnetic field, $H_{ext} + NM + N'M_s$. This additional negative field, $N'M_s$, can be of 0.5-1.0 T, depending on microstructural features and M_s ³⁴. Thus, if $H_{c,g} - H_{c,GB} < N'M_s$, the demagnetization of GB region will inevitably trigger an avalanche-like demagnetization process in the whole grain, driven by the local enhancement of the demagnetization field.

Conclusion

In summary, our results show that by electrochemically-controlled hydrogen charging/discharging the coercivity of the pinning-type $\text{Sm}_2\text{Co}_{17}$ -based magnet can be tuned by an unprecedented value of ~ 1.3 T, the highest value ever reported by a magneto-electric approach. In situ magneto-structural characterization and atomic-scale tracking of hydrogen atoms over the hierarchical microstructure reveals that the predominant change of the coercivity arises from the decoration of the grain boundaries with hydrogen atoms. These findings reveal, contrary to the conventional paradigm, a critical role of the grain boundaries in determining the coercivity in pinning-type magnets. Furthermore, these discoveries are anticipated to apply to other technologically important pinning-type magnets such as FePt and MnAl. Future performance-optimisation strategies should consider engineering of grain boundaries to enhance the coercivity of pinning-type magnets for the clean-energy applications. The demonstrated voltage-controlled and giant modification of the coercivity by hydrogen insertion (extraction) into grain boundaries also opens a way to various applications such as magneto-electric actuation or sensing in which large magneto-electric effect are needed.

Materials and methods

Materials and microstructure characterization. The Sm₂Co₁₇-type permanent magnets with dimensions of $\Phi 10$ mm \times 6 mm were purchased from Sigma-Aldrich (Stock No. 692832). The composition of the powder was analyzed by inductively-coupled plasma mass spectroscopy (**Table S1**) and its microstructure characterized by optical microscopy (KIT), powder X-ray diffraction with a Mo K _{α} , β source (Philips X'Pert Analysis, KIT), field-emission scanning electron microscope (SEM) equipped with energy dispersive X-ray spectroscopy and electron channeling contrast imaging (ECCI) (Zeiss Ultra 600/Merlin, both at KIT and MPIE), and transmission electron microscope (TEM, FEI Titan 80-300, KIT). Before optical and SEM characterization, the sample surface was mechanically polished. The preparation of TEM samples followed the ordinary procedure of cutting, lifting and milling using FIB/SEM dual beam system (FEI Strata 400 and Zeiss Auriga 60, KIT). The TEM observations were taken both with the c-axis of the crystal structure out of and parallel with the viewing planes.

Preparation of the Sm₂Co₁₇ powder electrode and the electrochemical set-up. To prepare the Sm₂Co₁₇ electrode, the as-received bulk sample was first charged with hydrogen atoms. The insertion of hydrogen atoms caused the expansion of the sample, and, consequently, the surface of the bulk sample collapsed into the very large particles. These particles were mixed with PVDF solution to form a slurry, which was then coated onto thin copper foils (thickness \sim 15 μ m). The slurry/Cu foil composite was then put into a homogeneous magnetic field to magnetically align the particles. Afterwards, it was further dried at room temperature for overnight. As the last step, the composite was compressed under a pressure of \sim 100 MPa to further fix the particles and to increase the electrical conductivity between Sm₂Co₁₇ particles and the Cu foil. We prepared the PVDF solution by dissolving PVDF powder in NMP solution at a mass ratio of 5:95 with stirring overnight.

The charging and discharging of the Sm₂Co₁₇ electrodes were carried out under potentiostatic control in a three-electrode electrochemical system (Autolab PGSTAT 302N, KIT). The working, the counter and the reference electrodes were the Sm₂Co₁₇ powder electrode, Pt wires and a pseudo Ag/AgCl electrode, respectively; the electrolyte was an aqueous electrolyte of 1 M KOH prepared from ultrapure water with a resistivity of \sim 18.2 M Ω (**Fig. S2**). The potential of the pseudo Ag/AgCl electrode is 0.300 \pm 0.002 V more positive than the standard Hg/HgO (1M KOH) electrode, and for comparison, all the voltages in the paper were converted to the Hg/HgO scale. According to the cyclic voltammogram of the SmCo_{7.35} electrode (**Fig. S3**), the voltages steps of -1.2V and -0.4 V were used to charge and discharge the sample, respectively.

In situ XRD measurement. The crystal structure of the Sm₂Co₁₇ electrode under the application of -1.2 V and -0.4 V was monitored by *in situ* XRD with a parallel beam laboratory rotating anode diffractometer (Mo K _{α} radiation) in transmission geometry. The transmission geometry allowed the detection of the entire volume of the SmCo₅ particles rather than only their surfaces. For *in situ* measurement, the Sm₂Co₁₇ electrode was attached to a glass plate (thickness \sim 0.1 mm) and then immersed in the 1 M KOH electrolyte in plastic bags. The counter and reference electrodes were the Pt wire and the pseudo Ag/AgCl electrode, respectively. Diffraction patterns were collected every 10 minutes with a Pilatus 300K-W area detector. NIST SRM660b LaB₆ powder was used for the detector

calibration and the determination of the instrumental resolution.

***In situ* SQUID measurement.** *In situ* magnetic measurement was carried out with a custom-built miniaturized Teflon electrochemical cell in a superconducting quantum interference device (SQUID, MPMS3, KIT) at room temperature. In the electrochemical cell, the Sm₂Co₁₇ electrode, Pt foil and pseudo Ag/AgCl electrode were the working, counter and reference electrodes, respectively. The electrolyte was 1 M KOH. The Sm₂Co₁₇ electrode and the Pt foil were attached to the flat surface of a plastic rod, and the reference electrode was threading through a capillary to determine the applied potential of the working electrode. The magnetic measurements were performed at the sealed mode of SQUID and with the applied magnetic field parallel to the surface of the Cu foil. The magnetic hysteresis loop of the bulk sample was measured with the magnetic field along the c-axis of the particles.

MOKE measurement

The magnetization reversal process was monitored by characterizing the magnetic domain structure under the external magnetic field using magneto-optical Kerr effect (MOKE) microscopy (Zeiss Axio Imager, D2m evico magnetics GmbH, TU Darmstadt). Before the MOKE observation, the sample was fully magnetized at a pulsed field of 6.8 T. Then, the magnetic domain structure was observed after applying a reversed magnetic field of 1.5 T, 2 T, 2.2 T, 2.5 T, 2.8 T, 3.0 T and 6.8 T. The magnetic field was applied parallel to c-axis of the matrix Sm₂Co₁₇ phase, and the images taken with the c-axis in the viewing plane. To enhance the image contrast, the non-magnetic background image was subtracted from the collected average image using KerrLab software.

APT measurement

For the atom probe tomography (APT, MPIE) measurement of hydrogen distribution, the Sm₂Co₁₇ electrode was charged at -1.2 V for ~2.5 hours in 0.1 M NaOD in D₂O (instead of H₂O) using the three-electrode system as described above. After the full charging, the sample was cleaned by ethanol and was transferred in 10 minutes to FIB chamber for the cutting, milling and lifting at room temperature (FEI Helios Nanolab 600/600i). 3-4 APT tips were prepared within 3-4 hours at room temperature. Annular milling was used to sharpen the needle-shaped morphology with a diameter less than ~100 nm. After that, a cleaning of the specimen at 5 kV was performed to remove the beam-damaged surface regions. The prepared tips were transferred into the load-lock chamber of APT, waited ~ 2 hours until the vacuum reached ~10⁻⁸ Pa (LEAP 3000 XHR), and then transferred into analysis chamber (~10⁻¹¹ Pa) at 70 K. We also acquired data on Cameca LEAP 5000XR, and only waited for half an hour before transferring the sample from APT load-lock to analysis chamber. The APT experiments were conducted using high-voltage mode with a pulse fraction of 15% at a base temperature of 70K, a pulse frequency of 200 kHz and an evaporation rate of 0.5. Atom probe data reconstruction and analysis were performed by CAMECA IVAS 3.8.4 software.

-
1. O. Gutfleisch, M. A. Willard, E. Brueck, C. H. Chen, S. Sankar, J. P. Liu. Magnetic materials and devices for the 21st century: stronger, lighter, and more energy efficient. *Adv. Mater.* **23**, 821-842 (2011).
 2. J.M.D. Coey. Hard magnetic materials: a perspective. *IEEE Trans. Magn.* **47**, 4671-4681 (2011).

3. K. Loewe, D. Benke, C. Kübel, T. Lienig, K.P. Skokov, O. Gutfleisch. Grain boundary diffusion of different rare earth elements in Nd-Fe-B sintered magnets by experiment and FEM simulation. *Acta Mater.* **124**, 421-429 (2016).
4. A.M. Gabay, M. Marinescu, W.F. Li, J.F. Liu, G.C. Hadjipanayis. Dysprosium saving improvement of coercivity in Nd-Fe-B sintered magnets by Dy₂S₃ additions. *J. Appl. Phys.* **109**, 083916 (2011).
5. Y. Dong, T.L. Zhang, Z.C. Xia, H. Wang, Z.H. Ma, X. Liu, W. Xia, J. M. D. Coey and C. B. Jiang. Dispersible SmCo₅ nanoparticles with huge coercivity. *Nanoscale* **11**, 16962 (2019).
6. J. Rial, P. Švec, E.M. Palmero, J. Camarero, P. Švec Sr, A. Bollero. Severe tuning of permanent magnet properties in gas-atomized MnAl powder by controlled nanostructuring and phase transformation. *Acta Mater.* **157**, 42-52 (2018).
7. S. Z., Y. Y. Wu, J. M. Wang, Y. X. Jia, T. L. Zhang, T.L. Zhang, C. B. Jiang. Realization of large coercivity in MnAl permanent-magnet alloys by introducing nanoprecipitates. *J. Magn. Magn. Mater.* **483**, 164-168 (2019).
8. O. Gutfleisch, J. Lyubina, K.H. Müller, L. Schultz. FePt hard magnets. *Adv. Eng. Mater.* **7**, 208-212 (2005).
9. M. Duerrschabel, M. Yi, K. Uestuener, M. Liesegang, M. Katter, H. J. Kleebe, B. Xu, O. Gutfleisch, L. Molina-Luna. Atomic structure and domain wall pinning in samarium-cobalt-based permanent magnets. *Nature Commun.* **8**, 54 (2017).
10. H. F. Mildrum, M. S.Hartings, K. J.Strnat, J. G. Tront. Magnetic Properties of the Intermetallic Phases Sm₂(Co, Fe)₁₇. *AIP Conf. Proc.* **10**, 618-622 (1973).
11. X.Y. Xiong, T. Ohkubo, T. Koyama, K. Ohashi, Y. Tawara, K. Hono, The microstructure of sintered Sm(Co_{0.72}Fe_{0.20}Cu_{0.055}Zr_{0.025})_{7.5} permanent magnet studied by atom probe. *Acta Mater.* **52**, 737-748 (2004).
12. O. Gutfleisch, K.H. Müller, K. Khlopkov, M. Wolf, A. Yan, R. Schaefer, T. Gemming, L. Schultz, Evolution of magnetic domain structures and coercivity in high-performance SmCo 2:17-type permanent magnets, *Acta Mater.* **54**, 997-1008 (2006).
13. H. Sepehri-Amin, J. Thielsch, J. Fischbacher, T. Ohkubo, T. Schrefl, O. Gutfleisch, K. Hono, Correlation of microchemistry of cell boundary phase and interface structure to the coercivity of Sm(Co_{0.784}Fe_{0.100}Cu_{0.088}Zr_{0.028})_{7.19} sintered magnets. *Acta Mater.* **126**, 1-10 (2017).
14. H. Kronmüller. Theory of nucleation field in inhomogeneous ferromagnets. *Phys. Stat. Sol. (b)* **144**, 385-396 (1987).
15. J. M. D. Coey. Coercivity in rare-earth iron permanent magnets. Clarendon Press (1996).
16. A.M.Gabay, M.Marinescu, J.F.Liu, G.C.Hadjipanayisa. Deformation-induced texture in nanocrystalline 2:17, 1:5 and 2:7 Sm-Co magnets. *J. Magn. Magn. Mater.* **321**, 3318-3323 (2009).
17. N.J. Yu, W.Y. Gao, M. Pan, H. F. Yang, Q. Wu, P. Y. Zhang, H.L. Ge. Influence mechanism of Fe content on the magnetic properties of Sm₂Co₁₇-type sintered magnets: Microstructure and microchemistry. *J. Alloys Comd.* **818**, 152908 (2020).
18. A. Molinari, Hahn H., R. Kruk, Voltage-control of magnetism in all-solid-state and solid/liquid magnetoelectric composites. *Adv. Mater.* 1806662 (2019).
19. A. Tan, M. Huang, C. O. Avci, F. Büttner, M. Mann, Wen Hu, C. Mazzoli, S. Wilkins, H. L. Tuller, G. S. D. Beach, Magneto-ionic control of magnetism using a solid-state proton pump. *Nature Mater.* **18**, 35-41 (2019).
20. X. L. Ye, H. K. Singh, H. B. Zhang, H. Gesswein, M. R. Chellali, R. Witte, A. Molinari, K. Skokov, O. Gutfleisch, H. Hahn, R. Kruk. Giant voltage-induced modification of magnetism in micron-scale ferromagnetic metals by hydrogen charging. *Nature Commun.* DOI:10.1038/s41467-020-18552-z.
21. D. A. Gilbert, A. J. Grutter. Hydrogen finds a home in ionic devices. *Nature Mater.* **18**, 7-8 (2019).
22. A. Pundt and R. Kirchheim. Hydrogen in metals: microstructural aspects. *Annu. Rev. Mater. Res.* **36**, 555-608 (2006).

-
23. M. Krautz, J. D. Moore, K. Skokov, J. Liu, C. S. Teixeira, R. Schäfer, L. Schultz, O. Gutfleisch. Reversible solid-state hydrogen-pump driven by magnetostructural transformation in the prototype system La (Fe, Si)₁₃H_y. *J. Appl. Phys.* **112**, 083918 (2012).
 24. Y.S. Chen, H.Z. Lu, J. Liang, A. Rosenthal, H. Liu, G. Sneddon, I. McCarroll, Z. Zhao, W. Li, A. Guo, J.M. Cairney. Observation of hydrogen trapping at dislocations, grain boundaries, and precipitates. *Science* **367**, 171–175 (2020).
 25. A. J. Breen , L. T. Stephenson , B. Sun, Y. Li , O. Kasian , D. Raabe, M. Herbig, B. Gault. Solute hydrogen and deuterium observed at the near atomic scale in high-strength steel. *Acta Mater.* **188**, 108-120 (2020).
 26. V. J. Araullo-Peters, B. Gault, S. L. Shrestha, L. Yao, M. P. Moody, S. P. Ringer, J. M. Cairney. Atom probe crystallography: Atomic-scale 3-D orientation mapping. *Scripta Mater.* **66**, 907-910 (2012).
 27. M. Palit, D.M. Rajkumar, S. Pandian, S.V. Kamat. Effect of grain size and magnetic properties of Sm₂(Co,Cu,Fe,Zr)₁₇ permanent magnets. *Mater. Chem. Phys.* **179**, 214-222 (2016).
 28. Y.Q.Wang, M. Yue, D.Wu, D.T. Zhang, W.Q. Liu, H.G. Zhang. Microstructure modification induced giant coercivity enhancement in Sm(CoFeCuZr)_z permanent magnets. *Scripta Mater.* **146**, 231-235 (2018).
 29. Y. Horiuchi, M. Hagiwara, M. Endo, N. Sanada, S. Sakurada. Influence of intermediate-heat treatment on the structure and magnetic properties of iron-rich Sm(CoFeCuZr)_z sintered magnets. *J. Appl. Lett.* **117**, 17C704 (2015).
 30. G. Yan, W. Xia, Z. Liu, R. Chen, C. Zhang, G. Wang, J. Liu, A. Yan. Effect of grain boundary on magnetization behaviors in 2:17 type SmCo magnet. *J. Magn. Magn. Mater.* **489**, 165459 (2019).
 31. E. Lectard, C. H. Allibert, R. Ballou. Saturation magnetization and anisotropy fields in the Sm(Co_{1-x}Cu_x)₅ phases. *J. Appl. Phys.* **75**, 6277-6279 (1994).
 32. T. Katayama, T. Shibata. Magnetocrystalline anisotropy constant in Sm(Co, Cu)₅ base Alloy. *Japanese J. Appl. Phys.* **12**, 762-764 (1973).
 33. H. Kronmuller. Micromagnetism of hard magnetic nanocrystalline materials. *Nanostructured Mater.* **6**, 157-168 (1995).
 34. W. Xia, Y. He, H. Huang, H. Wang , X. Shi, T. Zhang, T. Zhang, J. Liu, P. Stamenov, L. Chen, J.M. Coey, C.B. Jiang. Initial Irreversible Losses and Enhanced High - Temperature Performance of Rare - Earth Permanent Magnets. *Adv. Func. Mater.* **29**, 1900690 (2019).

Acknowledgements

The authors appreciate financial support from Deutsche Forschungsgemeinschaft under contract number HA 1344/34-1 (R.K, H.H.) and CRC/TRR 270, (L.S., K.S., O.G., BG) as well as Alexander von Humboldt Foundation (X.Y.). BG and LTS acknowledges financial support from the ERC-CoG-SHINE-771602. **Author contributions:** X.Y., R.K., H.H. conceived the project. X.Y. designed the experiments. X.Y. conducted material preparation and microstructural observation, built in situ electrochemical charging/discharging setup and conducted magnetic measurements; F.Y. conducted APT, part of SEM, assisted by L.T.S, and F.Y., B.G. processed APT data; L.S., X.Y. performed MOKE; H.G., X.Y. performed in-situ XRD; M.R.C. prepared TEM samples, discussed results, and D.W, W.W conducted TEM observation. K.S. and O.G contribute significantly to the interpretation of results. X.Y. wrote the initial draft and B.G., K.S., R.K. revised the manuscript. All authors participated in the discussions, contributed to improving the manuscript and approved the submitted manuscript. **Competing interests:** None. **Data and materials availability:** All data needed to evaluate the conclusions of the study are present in the paper or the supplementary materials.

Supplementary Materials:

Fig. S1 to S8

Table S1

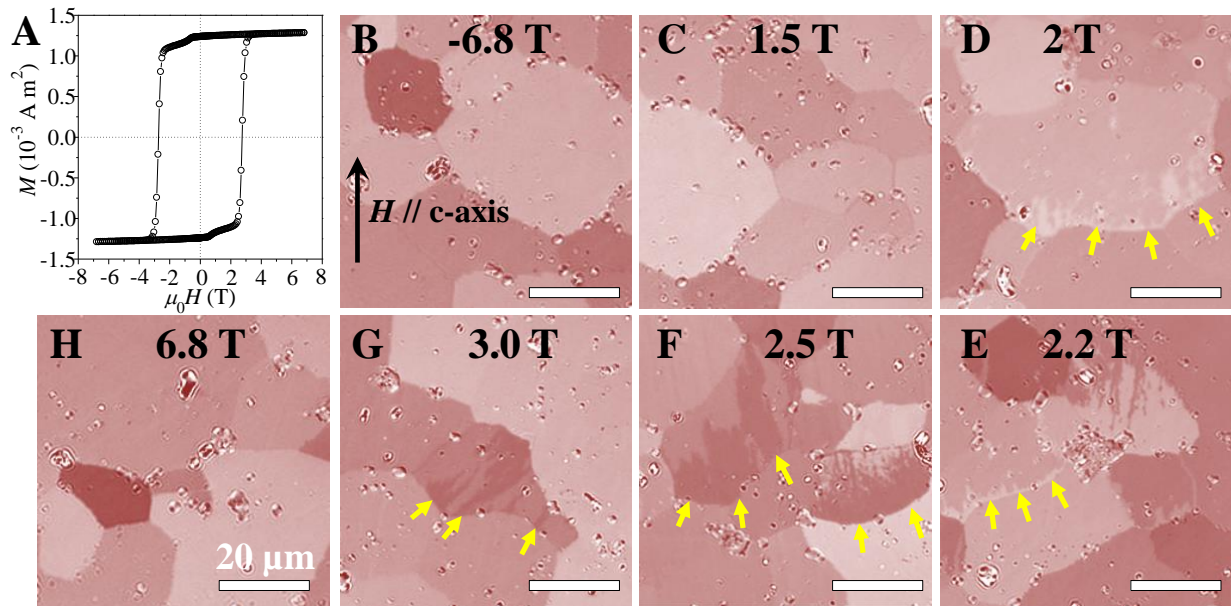


Fig. 1 Magneto-optical Kerr effect (MOKE) microscopy observation of the magnetization reversal process in $\text{Sm}_2\text{Co}_{17}$ -based magnet (A) Hysteresis loops of the bulk $\text{Sm}_2\text{Co}_{17}$ -type magnet. (B-H) MOKE observation of the magnetic domain structure under different demagnetization field from the magnetically-saturated state – the applied magnetic field is parallel to c-axis of crystal structure as indicated in (B).

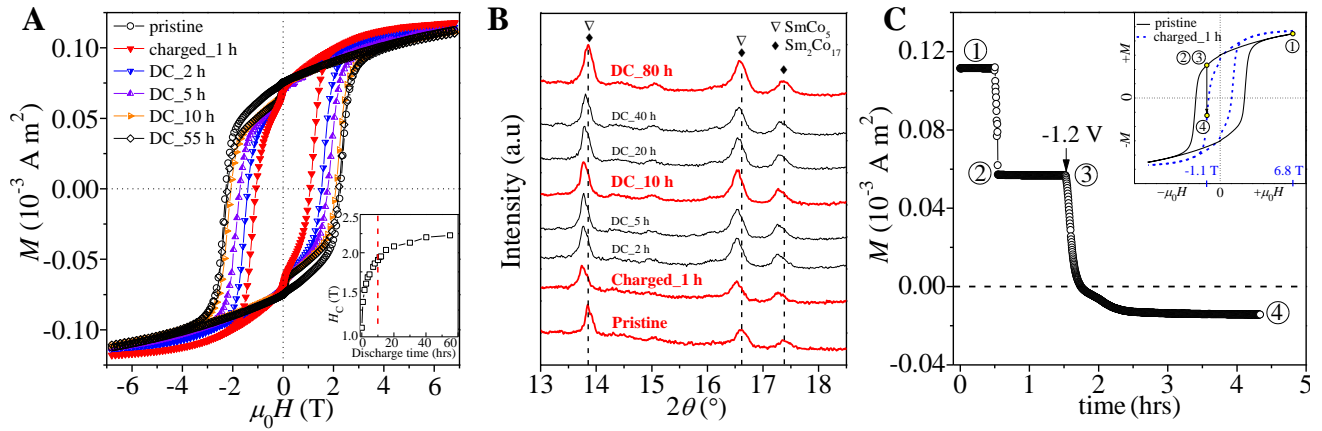


Fig. 2. Reversible modification of the coercivity in $\text{Sm}_2\text{Co}_{17}$ -based magnet by hydrogen charging/discharging and its dynamics. (A) Hysteresis loops of the as-prepared sample and those after hydrogen charging at -1.2 V for 1 hour (charged_1h) and after further discharging for 2 h (DC_2h), 5 h (DC_5h), 10 h (DC_10h) and 55 h (DC_55h). **Inset** shows the continuous change of the coercivity against the discharging time. (B) *In situ* XRD monitoring the evolution of the crystal structure of the as-prepared sample during charging and discharging, showing that within the first 10 hours of discharging the diffraction pattern remained nearly unchanged compared with the charged sample. (C) Time evolution of the magnetization in the as-prepared sample with the voltages switched to -1.2 V, showing the immediate response of magnetization reversal to voltage stimulus. Points ①, ②, ③, and ④ indicate different magnetization states as shown in the **inset**.

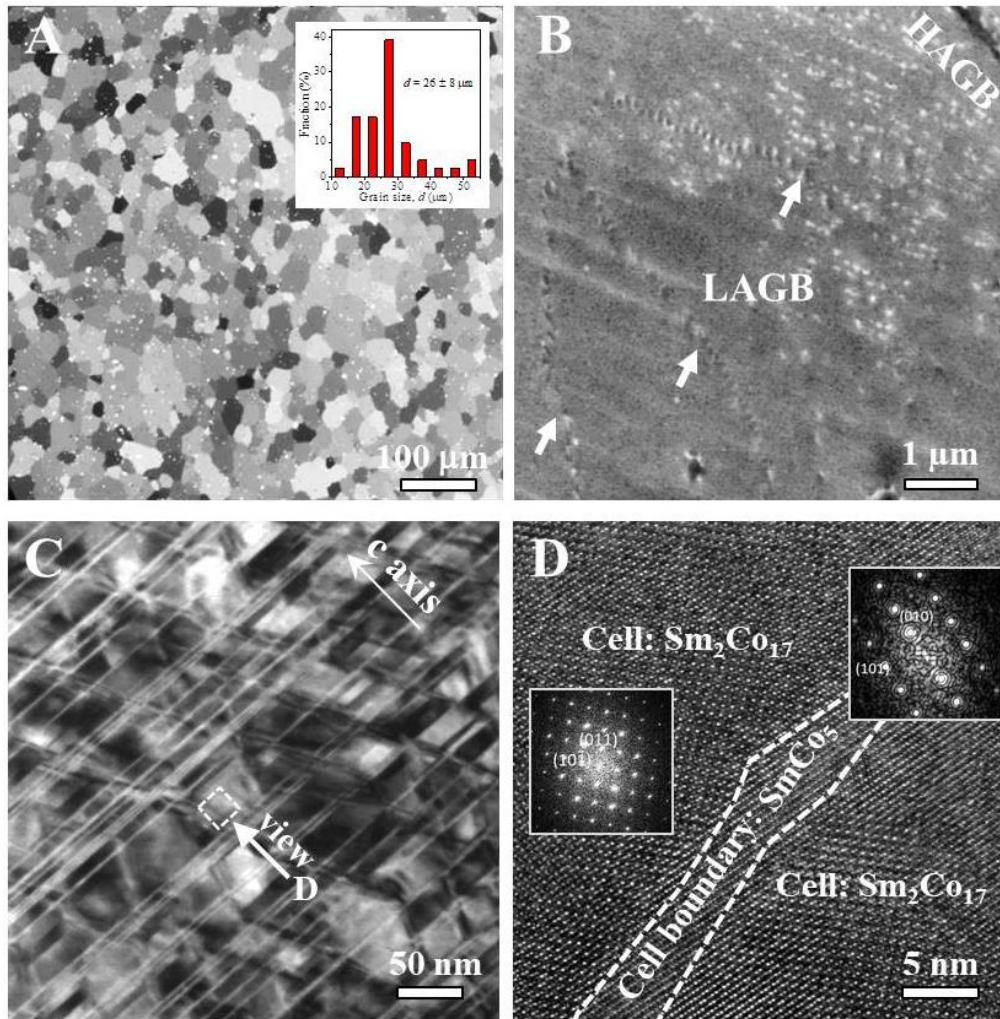


Fig.3. Multi-level multi-spectroscopy characterization of the hierarchical microstructure in $\text{Sm}_2\text{Co}_{17}$ -based magnet. (A) An optical microscopy image showing the polycrystalline grains with grain sizes $\sim 26 \mu\text{m}$. (B) An enlarged image of the crystal grain showing low-angle grain boundaries (LAGB) within the grain. (C) A bright-field TEM image within the grain showing the nano-scaled cellular structure, composed of the $\text{Sm}_2\text{Co}_{17}$ cell, the SmCo_5 cell boundary and the Zr-rich platelets. (D) A close-up on the cell and cell boundary by HRTEM and their Fourier transformation. The c-axis of the matrix phase in (C) and (D) is in and out of the viewing plane, respectively.

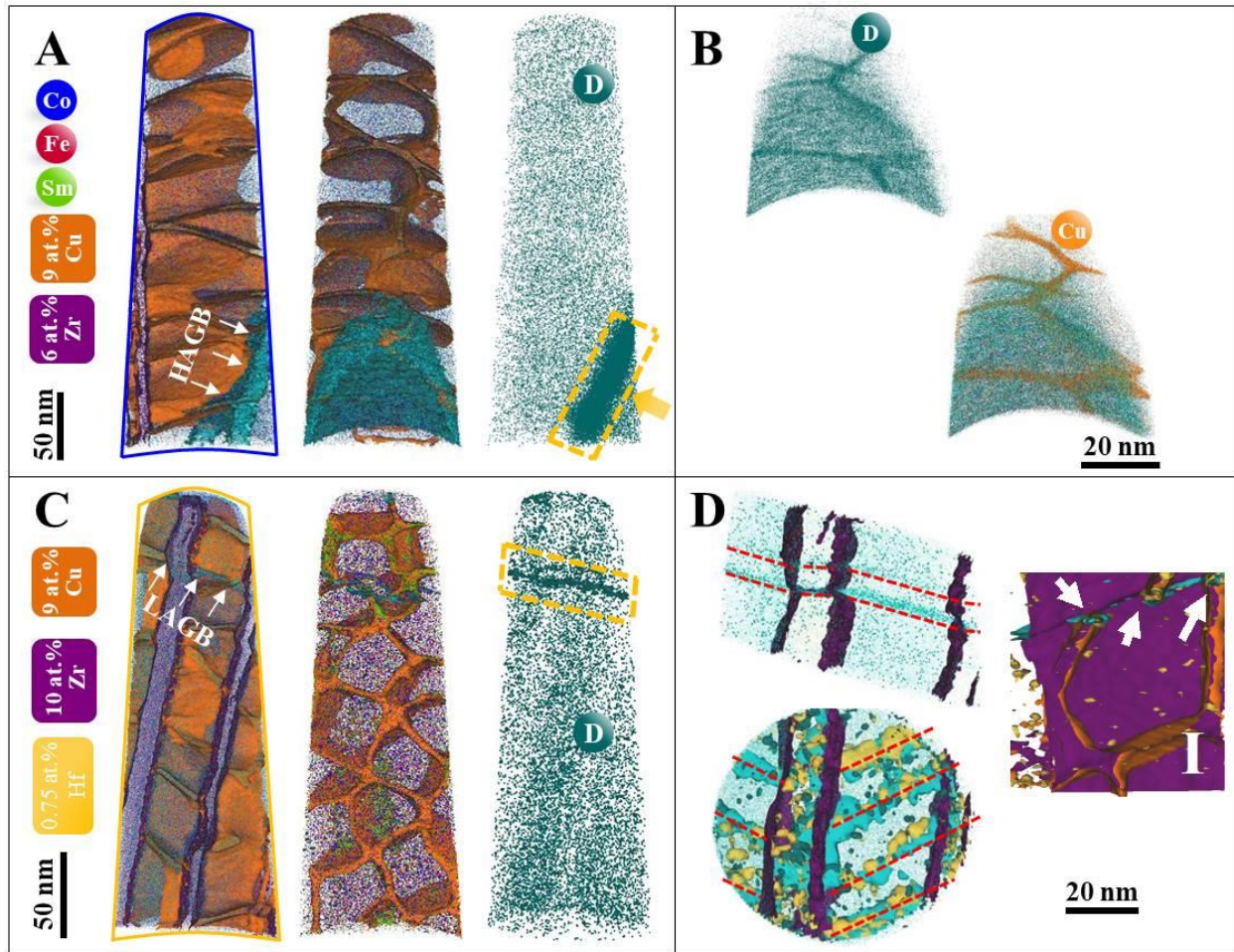


Fig. 4 Atomic-scale tracking of hydrogen/deuterium atoms within the microstructure in $\text{Sm}_2\text{Co}_{17}$ -based magnet. (A) 3D atom map of a deuterium-charged sample containing a high-angle grain boundary (HAGB). The sets of 9 at.% Cu and 6 at.% Zr iso-composition surfaces evidence the Cu-rich cell boundaries and the Z-phase; the distribution of deuterium reveals strong planar segregation near HAGB. (B) A face-on view on the distribution of D and Cu using 3.5 at.% D and 9 at.% Cu near the HAGB highlighting the co-location of D and Cu. Note the incomplete cellular structure and its abrupt stop at HAGB. (C) 3D atom map of a deuterium-charged specimen containing a low-angle grain boundary (LAGB). Note the disruption of the cellular structure adjacent to LAGB. The distribution of D shows the strong planar segregation at LAGB, the depletion at Zr-rich phase and no partitioning between cell and cell boundary. (D) A close-up using 0.35 at.% D, 0.75 at.% Hf and 4.5 at.% H iso-surfaces showing D segregation along a series of linear features interpreted as dislocations, each of which is connected to a cell edge; a close-up on the LAGB showing the direction connection of each dislocation to a cell boundary as indicated by white arrows (right side in D).